Palaeozoic cooling modulated by ophiolite weathering through organic carbon preservation

Palaeozoic cooling modulated by ophiolite weathering through organic carbon preservation

Joshua Murray[1], Oliver Jagoutz[1]

[1]Department of Earth, Atmospheric, and Planetary Sciences, Massachusetts Institute of Technology, Cambridge, MA 02139, USA

Corresponding author:
Joshua Murray
Massachusetts Institute of Technology,
77 Massachusetts Ave., 54-1124,
Cambridge, MA,
02139

joshmurr@mit.edu

Classification: Physical Sciences; Earth, Atmospheric, and Planetary Sciences

Keywords: Carbon, Tectonics, Clays, Glaciation, Earth, Climate, Weathering

Abstract

Ophiolite obductions in the tropics are coeval with Phanerozoic glaciations. The exposure of mafic and ultramafic rocks is thought to trigger cooling by increasing global weatherability. However, each Palaeozoic icehouse also coincides with a δ^{13}C increase of 3-5‰, interpreted as an increase in organic carbon burial, not weatherability. Here, we provide a framework that explains the tectonic forces behind Palaeozoic glaciations through increased organic carbon burial caused by the weathering of mafic and ultramafic lithologies in ophiolites. To evaluate the leverage ophiolite obduction has over organic carbon burial, we couple a mineral weathering model with a carbon box model. We show that the weathering of (ultra)mafic rocks can significantly enhance the preservation of organic carbon through the formation of high surface area smectite clays. The heightened organic carbon burial induced by an idealised ophiolite obduction causes ocean δ^{13}C to increase by ~3.7‰. The temporal evolution and magnitude of our modelled δ^{13}C excursion approximates Palaeozoic records. We present an analysis of shale geochemistry, which shows a correlation between ultramafic provenance and total organic carbon. Our results indicate that high surface area clays, formed during weathering of (ultra)mafic lithologies, exert a major control over Earth's long-term carbon cycle.

Main Text

Earth's climate is significantly controlled by the partial pressure of carbon dioxide (pCO_2) in the atmosphere (1). The major tectonic control(s) of Earth's pCO_2 on million-year timescales are volcanic outgassing (2), silicate weatherability (3), and/or organic carbon (OC) burial (4). The importance of mafic lithologies, uplift, and local climate for chemical weathering has motivated recent studies that show a temporal coincidence between ophiolite obduction in the tropics and icehouse climates (5-8). These studies argue that the obduction of mafic and ultramafic rocks (rich in Ca and Mg) raises Earth's weatherability, augmenting the flux of alkaline earth cations to the ocean and increasing carbonate precipitation for a given pCO_2.

The icehouse climates of the Palaeozoic are characterised by positive $\delta^{13}C$ excursions (see Methods). These records could be the result of weathering carbonate shelves following glacioeustatic marine regression (3). Alternatively, heightened OC burial could simultaneously explain both global cooling and positive $\delta^{13}C$ through a single feedback (9, 10) but has not been causally linked to the obduction of mafic and ultramafic lithologies in the tropics during times of glaciation (7, 8).

Over 99.5% of all OC is degraded before it is buried below the upper reactive layer of marine sediment (11). The fraction that is preserved is protected from remineralisation by adsorption on the surface of clay minerals and iron oxides. As such, clay species with high specific surface area (SSA) provide greater protection (12, 13). Shales rich in kaolinite, which has an SSA of 15 m^2/g, have systematically lower total organic carbon (TOC) levels than those rich in smectite, which has an SSA of ~800 m^2/g (14; **Fig. 1E**). As smectites are formed more readily under Mg-rich solutions and from Mg-rich bedrocks (15-18), we outline a pathway by which (ultra)mafic rock exposures alter the long-term carbon cycle through enhanced OC preservation. We evaluate the effects of ophiolite-derived clays and subsequent OC burial, in tandem with increased weatherability, and reconcile Palaeozoic glaciations with changes in $\delta^{13}C$ and surface lithology.

Mineral weathering model

We present a simple model of clay formation through individual mineral weathering reactions. As fresh rocks are exposed on the surface, their constituent minerals chemically weather, first in-situ and then during erosion and transportation to the continental shelf. The minerals formed during weathering and the rate of alteration depends upon the primary mineral, grain size, climate, microporosity, and co-occurring mineralogy (19). However, the ratio between mineral weathering rates remains approximately constant (20). By using the most common reaction pathways and using relative reaction rates, we simplify weathering reactions of different lithologies to a tractable representation of clay formation (see Methods).

We compiled the weathering reactions rates for eight common rock forming minerals. Peridotite, gabbro, and granite are treated as an aggregate of their constituent minerals and serve as ultramafic, mafic, and felsic end-members, respectively. We track the mineralogy and SSA of each rock with increasing degree of chemical weathering, ω, (**Fig. 1**). Results of our model show that ultramafic rocks, and to a lesser extent mafic rocks, rapidly form smectite clays from their Al-poor primary minerals, leading to peak SSA (250-775 m^2/g) sediments at $\omega = 10^{-3.6}$, before a decline in SSA as smectite is altered to silica and goethite with greater ω (**Fig. 1**). Felsic rocks weather more slowly due to their stable constituent minerals and the resulting kaolinite-rich sediment has low SSA (14-27 m^2/g), peaking around $\omega = 10^{-4.4}$ before vermiculite weathers to kaolinite (**Fig. 1**).

Carbon box model

The empirical relationship between SSA and TOC (**Fig. 1E**) provides a framework by which changes in lithology can force climate: mafic and ultramafic minerals create high SSA clays which increase the preservation potential of OC. Irrespective of whether the OC is pedogenic or, more likely, marine in origin (21), its preservation in siliciclastic deposits represents a transfer of carbon from the ocean-atmosphere system to the lithosphere. We adopt a linear function to describe the influence of changing SSA on OC preservation and proceed to model the carbon-cycle response to a change in surface lithology using a simple one-box model which couples the global fraction of exposed felsic, mafic, and ultramafic rocks, to clay mineralogy (**Fig. 1**), silicate

weathering flux, OC burial, ocean phosphorus, and pCO_2. We hold global sedimentation constant and the silicate weathering flux refers to the mass of carbon sequestered as carbonates due to the chemical weathering of silicate minerals and the associated Ca and Mg released (see Methods).

Ocean phosphorus is thought to play a critical role in OC burial through Earth history due to the limitations it places upon primary productivity (22). Over long timescales, if phosphorus is buried in organic matter according to the Redfield ratio, C:P of 106:1, OC burial cannot exceed the riverine flux of phosphorous, regardless of sedimentary SSA (22). However, preferential recycling of phosphorus from the sediment back into the ocean has been well documented. In stratigraphic sections of organic-rich shales and anoxic conditions C:P ratios increase up to tenfold, including C:P in mineral bound OC deposited during OAE-2 (23-26). Our model treats buried C:P ratio as a function of phosphorus in the ocean and we present model results with differing maximum burial values of C:P (see Methods). Our model is not intended to fully recreate the complexities of the global carbon cycle, particularly the feedbacks which operate on short timescales, but rather to gauge the implications of increasing the fraction of siliciclastic sedimentation derived from mafic and ultramafic regions.

To approximate an ophiolite obduction we force the carbon box model by increasing the global surface fraction of ultramafic and mafic rocks by 0.5% each over 2 Myr from an initial 0% and 4%, respectively. This agrees with observed obduction length of 5,000 km and overthrust of 300 km (7). The influence of different obduction lengths and ultramafic fractions over steady state $\delta^{13}C$ and pCO_2 are shown in **Fig. S2** and **Fig. S3**. To simulate the period over which tectonic uplift is equal to erosion, we maintain the amount of exposed ophiolite for 4 Myr, after which additional mafic and ultramafic lithologies decay exponentially (**Fig. 2A**).

In our model, the emplacement of mafic and ultramafic rocks results in a 61% increase in the mean SSA of global sediment from 56 m^2/g to 80 m^2/g (**Fig. 2B**). Assuming sufficient phosphorus recycling, the OC preservation associated with heighted SSA increases the OC burial flux from 73 MT/yr of C to 102 MT/yr (**Fig. 2C**). To reach steady state, pCO_2 decreases 3.7-fold (**Fig. S4C**) until the silicate weathering flux decreases from 127 MT/yr to 99 MT/yr. This cooling lowers ω from $1.9 \bullet 10^{-4}$ to $1.0 \bullet 10^{-4}$, which has a minor influence over SSA (**Fig. 2B, Fig. S4D**). The OC burial causes a 3.7‰ positive $\delta^{13}C$ excursion (**Fig. 2D**). Using a climate sensitivity of 3-4°C (27) yields mean global cooling of 6-8°C, comparable to the changes observed at the initiation of icehouse climates (28). Holding weatherability constant, making OC burial the sole driver of our carbon model, limits the pCO_2 decrease to 3.2-fold, corresponding to a 5-7°C cooling (**Fig. S5**).

If phosphorus is not recycled, OC burial becomes phosphorus-limited ~2 Myr after the onset of ophiolite obduction. This limitation is due to both a decrease in the riverine phosphorus flux as the silicate weathering flux decreases (**Fig. S6B**) and an increase in OC burial (**Fig. 2C**). In this scenario, OC burial is capped at 86 MT/yr by the riverine phosphorus flux. The isotopic excursion remains similar in magnitude, reaching 3.6‰, but is truncated by the phosphorus limitation, causing a rapid decrease in $\delta^{13}C$ to 1.8‰. The change in atmospheric pCO_2 is limited to a 2-fold decrease, which is reflected in both the silicate weathering flux and the degree of weathering, ω. We present intermediate values for maximum C:P of 106-150 in **Fig. 2**. For our obduction scenario, any buried C:P ratio greater than 142:1 yields identical model results for $\delta^{13}C$ and pCO_2 as the OC burial rate remains SSA-limited.

Alongside phosphorus, iron is thought to be a limiting nutrient in parts of the ocean (29). However, these elements are more abundant in mafic lithologies than felsic lithologies. Average mafic phosphorous concentrations are 1.5-2 times that of felsic rocks while mafic and ultramafic

iron concentrations are 3.6 and 5.3 times higher than felsic rocks, respectively (**Fig. S7**). If scavenged in the nearshore environment, the high concentrations of essential nutrients in mafic rocks could serve to locally fertilise the ocean and further increase the burial of OC, rather than limiting it. The impacts on the carbon cycle from combined ocean fertilisation and OC preservation could be greater and more abrupt than is discussed herein.

Geologic and geochemical evidence

We compiled measured carbon isotopes across the four major Palaeozoic ice ages. The timing and extent of each glaciation is not well constrained (see Methods) but is coeval with major ophiolite obductions (8, **Fig. S8).** We find that ophiolite obductions along longer suture zones coincide with greater $\delta^{13}C$ excursions (**Fig. 3A**). We show representative $\delta^{13}C$ excursions from carbonate sections for the end-Ordovician, Frasnian-Famennian, and end-Devonian in **Fig. 3B**. The isotopic evolution is comparable to that of our model results, showing a rapid increase, a prolonged high $\delta^{13}C$ state, prior to a more gradual decline (**Fig. 3B**). The end-Ordovician is well preserved in carbonate stratigraphy in Nevada, showing a singular plateau of ~4‰ with a rapid onset and decrease (30; **Fig. 3B**). The Frasnian-Famennian record consists of the two positive excursions of the Lower and Upper Kellewasser (31; **Fig. 3B**). The negative $\delta^{13}C$ shift between the Lower and Upper Kellewasser horizons is qualitatively similar to our phosphorus-limited model. The end-Devonian has been sampled extensively by drill cores in Iowa where it resembles the end-Ordovician excursion in both magnitude and shape (32; **Fig. 3B**). No single carbonate section captures the Permo-Carboniferous glaciation, which lasts at least 40 Myr and spans multiple ophiolite obductions (8). As such, we derive the magnitude of the excursion from a $\delta^{13}C$ fossil compilation (10) and add a spline fit with a smoothing parameter of 0.1 (**Fig. S8)**.

Isotopes of strontium and osmium have been used as proxies of silicate weathering. In both systems, mafic and ultramafic rocks are less radiogenic that their felsic counterparts with lower values of $^{87}Sr/^{86}Sr$ and $^{187}Os/^{188}Os$. Unfortunately, the Palaeozoic records of osmium are sparse and those present are aliased due to their resolution being coarser than the ocean residence time of osmium (e.g., 33, 34). Because the concentration of Sr in mafic and ultramafic rocks is lower than felsic lithologies, coupling our silicate weathering rates to Sr fluxes predicts a minor $^{87}Sr/^{86}Sr$ decrease from 0.7083 to 0.7080, substantially smaller than the Palaeozoic variations (Methods, **Fig. S9, S10**). The change we infer from our model highlights the first order control of strontium-rich continental rocks (35) and the inefficacy of $^{87}Sr/^{86}Sr$ as a diagnostic of ultramafic weathering. As Sr and Os weathering proxies are of limited use in evaluating our hypothesis, we use whole rock geochemistry to assess the influence of ophiolite weathering over OC burial.

Our framework for lithologically induced glaciations makes a clear prediction for the sedimentary rock record: sediments dominantly sourced from (ultra)mafic rocks should, on average, have higher TOC than those derived from felsic lithologies. Chromium has long been used as a tracer of ultramafic provenance in sedimentary rocks (36, 37) given its high concentration in the upper mantle (38) and relative immobility during weathering (39). We examine the geochemistry of 7820 shales of the Sedimentary Geochemistry and Paleoenvironents Project (SGP) for which Cr, Al_2O_3, and TOC data are present (40). We use Cr/Al ratios to remove the diluting effect of carbonate minerals. After discretising the data, we observe a systematic increase in the median and range of shale TOC with increasing Cr/Al ratio (**Fig. 4A,** Methods). We then inspect the temporal variation in Cr/Al of SGP shales and siltstones through the Phanerozoic and show the heightened occurrence of high Cr/Al samples during periods of glaciation (**Fig. 4B**). Median Cr/Al is 1.4 times greater and the Cr/Al at the 97.5^{th} percentile (2σ) is 4.2 times greater in

shales deposited during glaciations compared to shales of warmer periods. Given its short, 8 kyr residence time in the ocean (41), the Cr is likely derived from a proximal source rock, eroding essentially contemporaneously. The same trend is observed in Co/Al and Ni/Al, both insoluble trace element which are concentrated in mantle peridotites relative to the continental crust (**Fig. S11**). While the concentration of these elements in shales is additionally influenced by redox conditions and organic complexation, the fact that all three elemental ratios show similar trends supports our interpretation of an ultramafic signature. This correlation could be further bolstered by analysis of organo-mineral interfaces in Plio-Pleistocene sediments where an increase in detritus from the ultramafic terranes of the Southeast Asian islands around ~4 Ma is concurrent with an increase in TOC from 0.2-0.5 wt% to 1.0-1.8 wt% (42, 43).

TOC greater than ~15%, as observed in **Fig. 4A**, may be greater than can be adsorbed to mineral surfaces, and requires a combination of both high SSA and an anoxic environment (44). Even ignoring those data exceeding 15 wt% TOC, the sedimentary geochemistry supports the observation that the shales with a larger ultramafic component, on average, preserve a greater fraction of OC and that those shales occur more frequently during glacial periods (**Fig. 4, Fig. S11**).

Alongside the geochemical correlation in **Fig. 4**, we see evidence of ultramafic detritus (notably Cr-spinel) and slab breakoff closely preceding each Palaeozoic glaciation (**Fig. S12-14**). While Cr-spinel provides direct evidence of ophiolite weathering, slab processes may be governing the transport of high-SSA clays. While we treat ω as a global value, dependent only upon temperature, ω is high in areas with high chemical weathering rates and low erosion rates, where thick regoliths develop and smectite clays are further altered into iron oxides (5, 16). Slab breakoff would cause rapid uplift, enhanced erosion, lower ω and an increase in high-SSA sedimentation. The positive feedbacks between uplift, weathering, and erosion may cause punctuated cooling on timescales much faster than plate convergence.

In summary, through the framework of OC burial, we reconcile the theory of ophiolite-induced cooling with carbon isotope excursions across Palaeozoic glaciations. Our model calculations, the $\delta^{13}C$ isotopic record, and shale geochemistry all provide evidence to support the hypothesis that OC preservation by high SSA clays is a significant pathway by which ophiolite obduction disrupts the carbon cycle. The influence of tectonically driven clay formation and subsequent increased OC preservation, could extend far beyond Phanerozoic pCO_2 and be relevant for ocean anoxia, great oxidation event(s), and the initiation of snowball Earth (45–47).

Acknowledgements

We thank D. Rothman, and F. Macdonald for their insight, particularly in respect to the carbon cycle and its isotopic record. We thank M. Follows for a valuable discussion on dissolved oxygen and remineralisation. Funding for this work came from NSF EAR 1925863.

Author Contributions

J.M. and O.J. conceptualised the research. J.M. led modelling and statistical methods. J.M. and O.J. were responsible for data analysis, writing, and editing.

Competing Interests

The authors declare no competing interests.

Figures

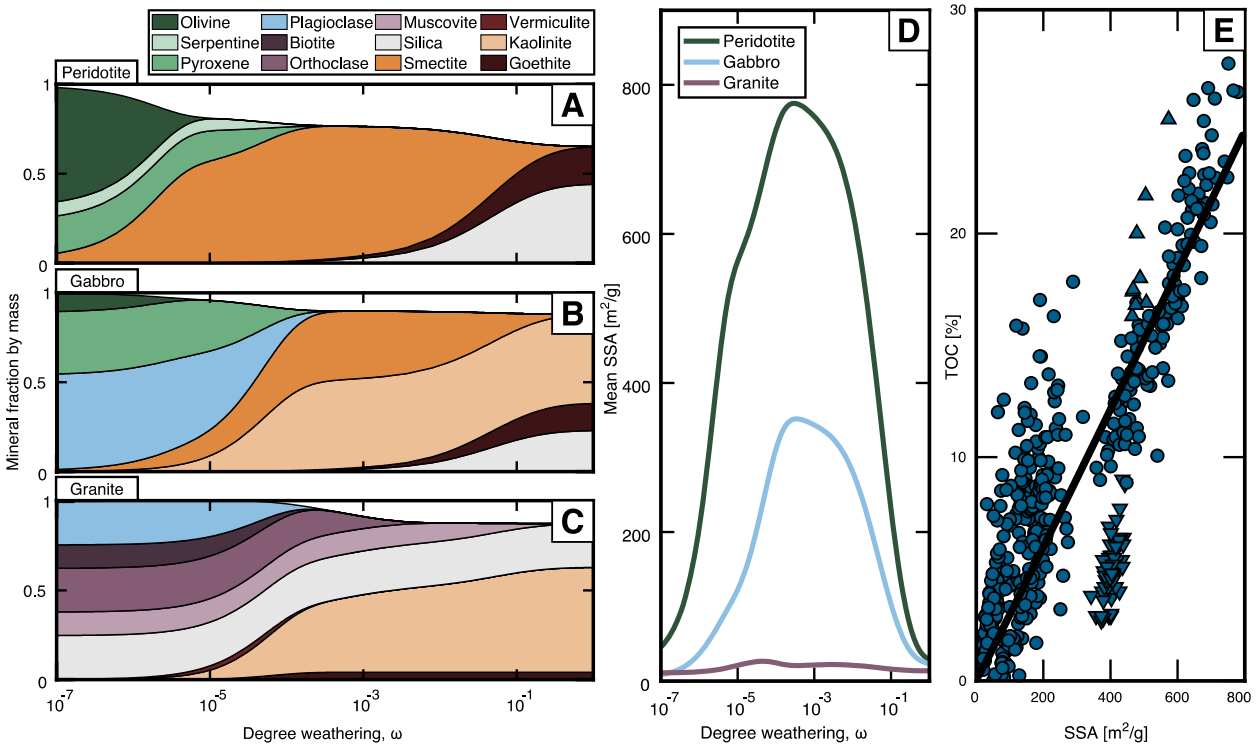

Figure 1: Relationships between primary lithology, modelled weathering products, SSA, and TOC. A) Modelled weathering of peridotite (lherzolite) with 70% olivine, 20% pyroxene, and 10% serpentine; B) Modelled weathering of gabbro with 60% plagioclase, 30% pyroxene, and 10% olivine. C) Modelled weathering of granite with 25% plagioclase, 25% orthoclase, 12.5% muscovite, 12.5% biotite, and 25% quartz. In panels A-C, mineral fraction is given as the fraction of the initial mass and progresses with increasing degree of weathering, ω (shown on a log scale). Relative weathering rates are given in **Table S1** (Methods). D) SSA of the bulk rock in panels A-C as the weathering reaction progresses. E) Compilation of SSA and TOC values. Downward pointing triangles represent data in which the authors attribute TOC loss to bioturbation. Upward pointing triangles represent data in which the authors document anoxia as contributing to high TOC values. The black line is a correlation consistent with monolayer equivalent adsorption of OC. We use this correlation to couple SSA to TOC (see Methods). The same data are reproduced in **Fig. S1** differentiated by the sample location.

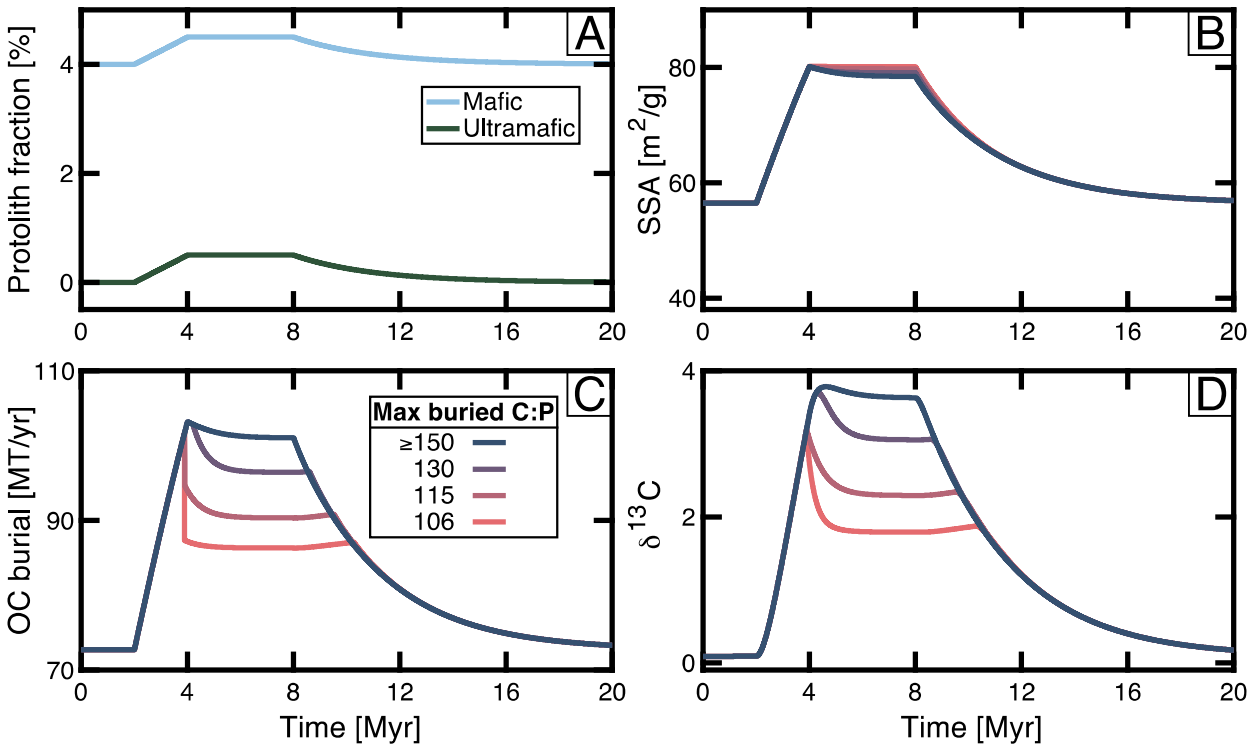

Figure 2: Model results from an idealised ophiolite obduction. Line colour reflects maximum C:P ratio in buried sediment (see Methods). A) Fraction of mafic and ultramafic lithologies on Earth's surface. Felsic lithologies provide the remaining percentage. B) Mean SSA of silicate weathering products. C) Change in organic carbon burial as a result of the increased average SSA D) Evolution of ocean $\delta^{13}C$ as OC burial changes.

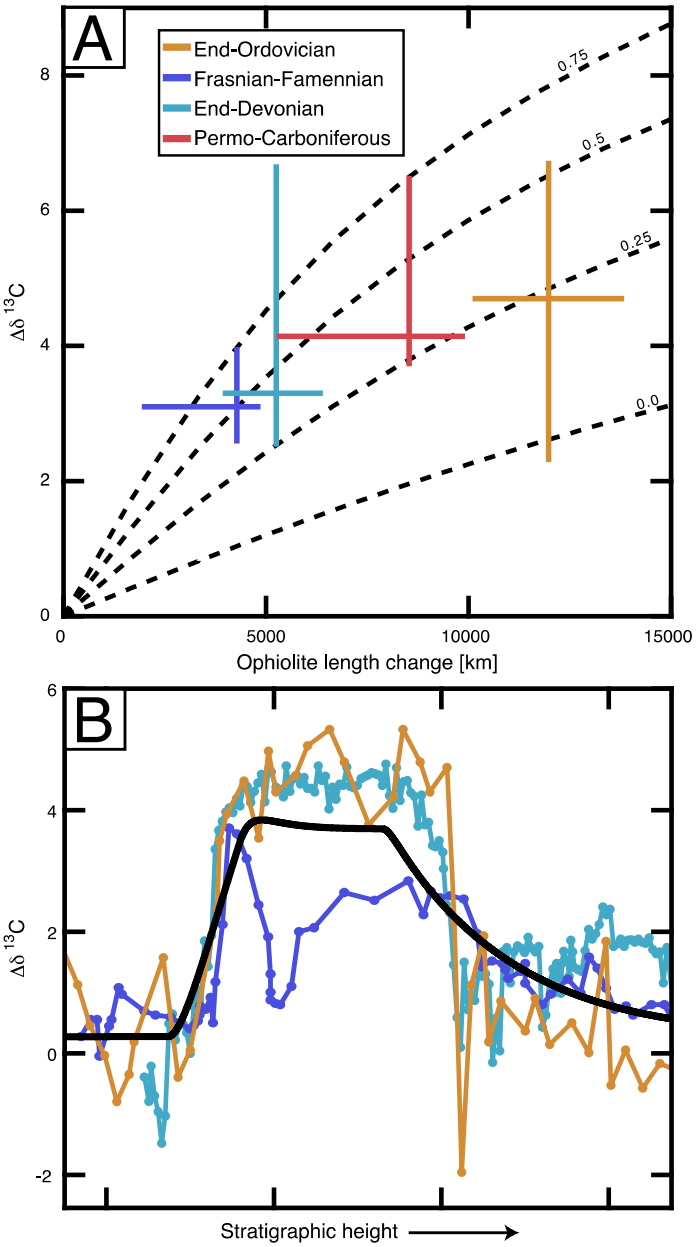

Figure 3: Comparison to the Palaeozoic $\delta^{13}C$ record. **A)** Magnitude of $\delta^{13}C$ excursions and changes in ophiolite length across the four Palaeozoic glaciations. The coloured lines reflect 1σ ranges of $\delta^{13}C$ excursions and ophiolite length changes. The intersection of the lines represents the median $\delta^{13}C$ excursion and ophiolite length change. Change in ophiolite length is derived from the sutures of (8). Our compilation of $\delta^{13}C$ excursions (**Table S5**, Methods), are used to constrain the magnitude of $\delta^{13}C$ excursions across the end-Ordovician (n=10), Frasnian-Famennian (n=8), and end-Devonian (n=10). The Permo-Carboniferous is not represented by a single stratigraphic section. Instead, we derive the size of the excursion from a comparison of brachiopod $\delta^{13}C$ values at the onset of the excursion (n = 30) to $\delta^{13}C$ values at the height of the excursion (n = 70) (10; see Methods and **Fig. S8**). Black dashed lines are our modelled changes in ocean $\delta^{13}C$ as a function of the length and ultramafic fraction of the weathering ophiolite (0-0.75). **B)** Example $\delta^{13}C$ isotope excursions from the end-Ordovician, Frasnian-Famennian, and end-Devonian glaciations, using the same colour scheme as **Fig. 3A** (30-32). Overlain in black is the modelled isotopic excursion without P limitation (**Fig. 2D**).

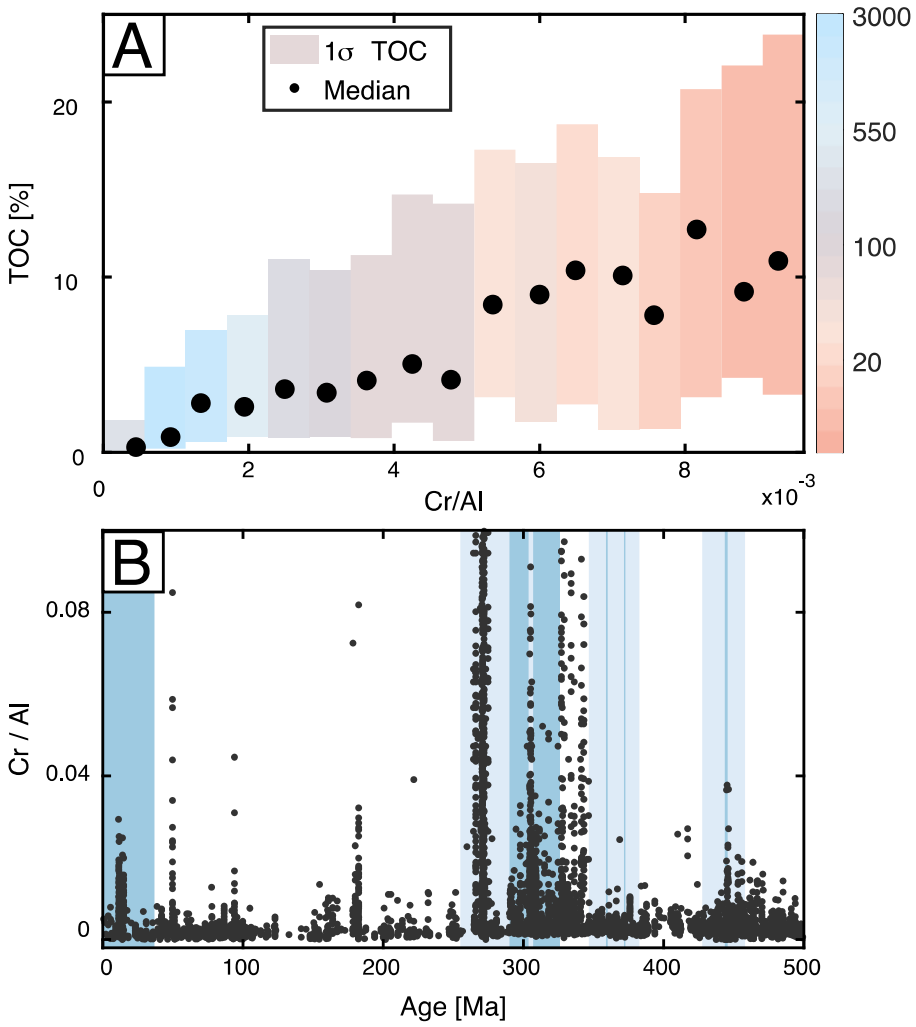

Figure 4: Analysis of SGP shale and siltstone geochemistry. **A)** Binned mean and standard deviation of SGP samples: horizontal axis is the ratio of Cr to Al, vertical axis represents TOC. Coloured boxes represent the single standard deviation of TOC for a given Cr/Al binned range. Black points show the median within the given bin. The colour of each rectangle denotes the number of samples contributing to the mean and standard deviation. At Cr/Al values exceeding 10^{-2}, the data are sparse and the relationship breaks down. This is likely caused by sorting which concentrates chromite in coarser, clay-poor sediments. **B)** Cr/Al of SGP samples through the Phanerozoic overlain on Phanerozoic glaciations. Dark blue bars show short end-member chronologies of glaciation, whereas pale blue bars show prolonged end-member chronologies (Methods, **Table S3**). Data continue above the limits of the y axis, particularly around the Permo-Carboniferous.

References

1. T. Owen, R. D. Cess, V. Ramanathan. Enhanced CO_2 greenhouse to compensate for reduced solar luminosity on early Earth. *Nature.* ***277***, 640-642 (1979).
2. N. R. McKenzie et al. Continental arc volcanism as the principal driver of icehouse-greenhouse variability. *Science.* ***352***, 444-447 (2016).
3. L.R. Kump et al. A weathering hypothesis for glaciation at high atmospheric pCO_2 during the Late Ordovician. *Palaeogeography, Palaeoclimatology, Palaeoecology.* ***152***, 173-187 (1999).
4. V. Galy et al. Efficient organic carbon burial in the Bengal fan sustained by the Himalayan erosional system. *Nature.* ***450***, 407-410 (2007).
5. C. Dessert, B. Dupré, J. Gaillardet, L. M. François, C. J. Allegre. Basalt weathering laws and the impact of basalt weathering on the global carbon cycle. *Chemical Geology.* ***202***, 257-273 (2003).
6. A. J. West, A. Galy, M. Bickle. Tectonic and climatic controls on silicate weathering. *Earth and Planetary Science Letters.* ***235***, 211-228 (2005): 211-228.
7. O. Jagoutz, F. A. Macdonald, L. Royden. Low-latitude arc–continent collision as a driver for global cooling. *Proceedings of the National Academy of Sciences.* ***113***, 4935-4930 (2016).
8. F. A. Macdonald, N. L. Swanson-Hysell, Y. Park, L. Lisiecki, O. Jagoutz. Arc-continent collisions in the tropics set Earth's climate state. *Science.* ***364***, 181-184 (2019).
9. L. R. Kump, M. A. Arthur. Interpreting carbon-isotope excursions: carbonates and organic matter. *Chemical Geology.* ***161***, 181-198 (1999).
10. E. L. Grossman et al. Glaciation, aridification, and carbon sequestration in the Permo-Carboniferous: the isotopic record from low latitudes. *Palaeogeography, Palaeoclimatology, Palaeoecology.* ***268***, 222-233 (2008).
11. J. I. Hedges, R. G. Keil. Sedimentary organic matter preservation: an assessment and speculative synthesis. *Marine chemistry.* ***49***, 81-115 (1995).
12. K. Lalonde, A. Mucci, A. Ouellet, Y. Gélinas. Preservation of organic matter in sediments promoted by iron. *Nature.* ***483***, 198-200 (2012).
13. J. D. Hemingway et al. Mineral protection regulates long-term global preservation of natural organic carbon. *Nature.* ***570***, 228-231 (2019).
14. M. J. Kennedy, D. R. Pevear, R. J. Hill. Mineral surface control of organic carbon in black shale. *Science.* ***295***, 657-660 (2002).
15. H. Harder. The role of magnesium in the formation of smectite minerals. *Chemical Geology.* ***10***, 31-39 (1972).
16. Nahon, D., F. Colin, and Y. Tardy. "Formation and distribution of Mg, Fe, Mn-smectites in the first stages of the lateritic weathering of forsterite and tephroite." *Clay Minerals* 17, no. 3 (1982): 339-348.
17. Brigatti, Maria Franca, and Luciano Poppi. "'Corrensite-like minerals' in the Taro and Ceno Valleys, Italy." *Clay minerals* 19, no. 1 (1984): 59-66.
18. de Obeso, Juan Carlos, and Peter B. Kelemen. "Major element mobility during serpentinization, oxidation and weathering of mantle peridotite at low temperatures." *Philosophical Transactions of the Royal Society A* 378, no. 2165 (2020): 20180433.
19. B. B. Velde, A. Meunier. *The origin of clay minerals in soils and weathered rocks*. (Springer Science & Business Media, 2008).
20. M. A. Velbel. Constancy of silicate-mineral weathering-rate ratios between natural and experimental weathering: implications for hydrologic control of differences in absolute rates. *Chemical Geology.* ***105***, 89-99 (1993).
21. Blattmann, Thomas M., Zhifei Liu, Yonghua Zhang, Yulong Zhao, Negar Haghipour, Daniel B. Montluçon, Michael Plötze, and Timothy I. Eglinton. "Mineralogical control on the fate of continentally derived organic matter in the ocean." *Science* 366, no. 6466 (2019): 742-745.
22. Laakso, Thomas A., and Daniel P. Schrag. "Regulation of atmospheric oxygen during the Proterozoic." *Earth and Planetary Science Letters* 388 (2014): 81-91.
23. Li, Yanfang, Tongwei Zhang, Geoffrey S. Ellis, and Deyong Shao. "Depositional environment and organic matter accumulation of Upper Ordovician–Lower Silurian marine shale in the Upper Yangtze Platform, South China." *Palaeogeography, Palaeoclimatology, Palaeoecology* 466 (2017): 252-264.
24. Percival, L. M. E., D. P. G. Bond, M. Rakociński, L. Marynowski, A. V. S. Hood, T. Adatte, J. E. Spangenberg, and K. B. Föllmi. "Phosphorus-cycle disturbances during the Late Devonian anoxic events." *Global and planetary change* 184 (2020): 103070.

25. Beil, Sebastian, Wolfgang Kuhnt, Ann Holbourn, Florian Scholz, Julian Oxmann, Klaus Wallmann, Janne Lorenzen, Mohamed Aquit, and El Hassane Chellai. "Cretaceous oceanic anoxic events prolonged by phosphorus cycle feedbacks." *Climate of the Past* 16, no. 2 (2020): 757-782.
26. Löhr, S. C., and M. J. Kennedy. "Organomineral nanocomposite carbon burial during Oceanic Anoxic Event 2." *Biogeosciences* 11, no. 18 (2014): 4971-4983.
27. S. C. Sherwood, S. Bony, J.-L. Dufresne. Spread in model climate sensitivity traced to atmospheric convective mixing. *Nature. **505***, 37-42 (2014).
28. R. M. DeConto et al. Thresholds for Cenozoic bipolar glaciation. *Nature. **455***, 652-656 (2008).
29. C. M. Moore et al. Processes and patterns of oceanic nutrient limitation. *Nature Geoscience. **6***, 701-710 (2013).
30. LaPorte, D. F., C. Holmden, W. P. Patterson, J. D. Loxton, M. J. Melchin, C. E. Mitchell, S. C. Finney, and H. D. Sheets. "Local and global perspectives on carbon and nitrogen cycling during the Hirnantian glaciation." *Palaeogeography, Palaeoclimatology, Palaeoecology* 276, no. 1-4 (2009): 182-195.
31. Buggisch, Werner, and Michael M. Joachimski. "Carbon isotope stratigraphy of the Devonian of Central and Southern Europe." *Palaeogeography, Palaeoclimatology, Palaeoecology* 240, no. 1-2 (2006): 68-88.
32. Stolfus, Brittany M., Bradley D. Cramer, Ryan J. Clark, Nicholas J. Hogancamp, James E. Day, Stephanie A. Tassier-Surine, and Brian J. Witzke. "An expanded stratigraphic record of the Devonian-Carboniferous boundary Hangenberg biogeochemical Event from Southeast Iowa (USA)." *Bulletin of Geosciences* 95, no. 4 (2020).
33. Finlay, Alexander J., David Selby, and Darren R. Gröcke. "Tracking the Hirnantian glaciation using Os isotopes." *Earth and Planetary Science Letters* 293, no. 3-4 (2010): 339-348.
34. Percival, L. M. E., David Selby, D. P. G. Bond, Michal Rakociński, Grzegorz Racki, Leszek Marynowski, Thierry Adatte, J. E. Spangenberg, and K. B. Föllmi. "Pulses of enhanced continental weathering associated with multiple Late Devonian climate perturbations: Evidence from osmium-isotope compositions." *Palaeogeography, palaeoclimatology, palaeoecology* 524 (2019): 240-249.
35. Edmond, J. M. "Himalayan tectonics, weathering processes, and the strontium isotope record in marine limestones." *Science* 258, no. 5088 (1992): 1594-1597.
36. Garver, J. I., P. R. Royce, and T. A. Smick. "Chromium and nickel in shale of the Taconic foreland; a case study for the provenance of fine-grained sediments with an ultramafic source." *Journal of Sedimentary Research* 66, no. 1 (1996): 100-106.
37. Hiscott, Richard N. "Ophiolitic source rocks for Taconic-age flysch: Trace-element evidence." *Geological Society of America Bulletin* 95, no. 11 (1984): 1261-1267.
38. Workman, Rhea K., and Stanley R. Hart. "Major and trace element composition of the depleted MORB mantle (DMM)." *Earth and Planetary Science Letters* 231, no. 1-2 (2005): 53-72.
39. J. Viers, B. Dupré, J. Gaillardet. Chemical composition of suspended sediments in World Rivers: New insights from a new database. *Science of the Total Environment. **407***, 853-868 (2009).
40. U. C. Farrell, et al. The sedimentary geochemistry and paleoenvironments project. *Geobiology. **19***, 545-556 (2021).
41. Broecker, Wallace S., and Tsung-Hung Peng. *Tracers in the Sea*. Vol. 690. Palisades, New York: Lamont-Doherty Geological Observatory, Columbia University, 1982.
42. Bayon, Germain, Martin Patriat, Yves Godderis, Anne Trinquier, Patrick De Deckker, Denise K. Kulhanek, Ann Holbourn, and Yair Rosenthal. "Accelerated mafic weathering in Southeast Asia linked to late Neogene cooling." *Science Advances* 9, no. 13 (2023): eadf3141.
43. Rosenthal, Y., Holbourn, A.E., Kulhanek, D.K., Aiello, I.W., Babila, T.L., Bayon, G., Beaufort, L., Bova, S.C., Chun, J.-H., Dang, H., Drury, A.J., Dunkley Jones, T., Eichler, P.P.B., Fernando, A.G.S., Gibson, K.A., Hatfield, R.G., Johnson, D.L., Kumagai, Y., Li, T., Linsley, B.K., Meinicke, N., Mountain, G.S., Opdyke, B.N., Pearson, P.N., Poole, C.R., Ravelo, A.C., Sagawa, T., Schmitt, A., Wurtzel, J.B., Xu, J., Yamamoto, M., and Zhang, Y.G., 2018. Site U1482. In Rosenthal, Y., Holbourn, A.E., Kulhanek, D.K., and the Expedition 363 Scientists, Western Pacific Warm Pool. Proceedings of the International Ocean Discovery Program, 363: College Station, TX (International Ocean Discovery Program).
44. Kennedy, Martin J., and Thomas Wagner. "Clay mineral continental amplifier for marine carbon sequestration in a greenhouse ocean." *Proceedings of the National Academy of Sciences* 108, no. 24 (2011): 9776-9781.
45. L. M. E. Percival et al. Phosphorus-cycle disturbances during the Late Devonian anoxic events. *Global and Planetary Change. **184***, 103070 (2020).

46. M. Kennedy, M. Droser, L. M. Mayer, D. Pevear, D. Mrofka. Late Precambrian oxygenation; inception of the clay mineral factory. *Science*. ***311***, 1446-1449 (2006).
47. D. P. Schrag, R. A. Berner, P. F. Hoffman, G. P. Halverson. On the initiation of a snowball Earth. *Geochemistry, Geophysics, Geosystems*. ***3***, 1-21 (2002).

Methods

Mineral weathering

The weathering of igneous minerals is simplified to a balanced chemical equation from primary mineral to its most common weathering product. We allow the secondary mineral to further weather if those reactions are commonly reported. We treat quartz, kaolinite, and goethite as stable. In nature, weathering reactions are more complicated than represented here. For example, clays formed in weathering ophiolites can be found as purely smectite (often stevensite or montmorillonite) (17); however, chlorite can be found interlayered with smectite, potentially formed during hydrothermal processes or as an intermediate weathering product (16). In order to consider siliciclastic mineralogy on a global scale, we idealise the weathering of each mineral independently and ignore the influence of co-occurring species. The idealised weathering reactions for each mineral are given in the SI with discussions of the simplifications we have made. We use chemical compositions in order to convert modal abundances to mass fractions (**Fig. 1**).

Weathering rates are dependent not only upon the mineralogy but also upon climate and physical erosion rates. Fortunately, the ratio of weathering rates between different minerals has been shown to be broadly constant across laboratory and field experiments (20), allowing us to simplify our model and use only relative weathering rates. The ratio of mineral alteration rates is given in **Table S1**. Our weathering model follows the progression of alteration reactions from primary to secondary (and tertiary where necessary) where the rate of the alteration of mineral A to mineral B is proportional to the inverse square root of the mean age of the reactant mineral (44):

$$dC_b/dt \propto k_a C_a \omega_a^{-1/2} \quad \text{(M1)}$$

Where k_a is the rate ratio of mineral A (**Table S1**), ω_a is the normalised age of mineral A, C_a is the fraction of mineral A present in the rock. We model the reaction numerically, updating the age and concentration of minerals A, B, (and C where necessary). Because the weathering rates are constructed relative to one another and are not absolute, ω reflects a normalised age, such that by $\omega = 1$ all reactions are complete and only silica, kaolinite, and goethite remain (**Fig. 1**). ω also serves as the degree of weathering in our carbon model (Eq. M11, M14).

We apply our weathering model to three igneous rock compositions: ultramafic, mafic, and felsic. The mineralogy of those initial, igneous compositions is given in **Table S2**. Mineral abundances are given as modal abundance and converted to mass to show chemical depletion. We then convert mass to SSA by the values in **Table S2**. Primary minerals are assigned an SSA of 0.1 m^2/g except for serpentine which is 8 m^2/g (48), and muscovite which has an illite SSA of 80 m^2/g (49).

SSA-TOC relationship

In order to couple SSA to TOC, we derive an empirical relationship between the two. We compiled 483 analyses of both SSA and TOC in shales across four continents (**Table S6**). Only those studies which used ethylene glycol monoethyl ether (EGME) for SSA analyses were selected due to the ability of both internal and external surface area to preserve organic carbon. We seek a best-fit function of the form:

$$TOC = a \cdot SSA^b \quad \text{(M2)}$$

However, b is close to 1 for most fit parameters and as such we simplify our idealised relationship to a proportionality:

$$\mathrm{TOC} = a \cdot \mathrm{SSA} \tag{M3}$$

The value of a is derived by a weighted linear regression of the SSA and TOC values in **Table S6**. Weights are proportional to the sum of the normalised Euclidean distances between the sample point and all other points (Eq. M4).

$$w_i \propto \sum \sqrt{\left(\frac{toc_i - toc_j}{\overline{toc}}\right)^2 + \left(\frac{ssa_i - ssa_j}{\overline{ssa}}\right)^2} \tag{M4}$$

This yields a = 0.0306 g/m^2. Giving a function which maps from sediment SSA to TOC. This relationship is consistent with preservation approximately equivalent to monolayer loading of TOC on clays (11; 44). We show the data and best fit line in **Fig. 1E**. We explore the dependence upon our SSA-TOC relationship in **Fig. S15** using values of coefficients a and b.

While mineral protection is a major control on OC burial on the continental margin (11,13,14), treating TOC solely as a function of SSA is an oversimplification. We ignore here the effects of temperature, sedimentation rate, and bottom water oxygen concentration. High sedimentation rates can lower the time over which OC is exposed to oxygen, increasing preservation (11). Similarly, ocean anoxia can significantly reduce remineralisation rates and raise TOC concentrations above monolayer equivalent values (44). The effects of temperature on OC preservation may be a feedback which is not represented within our model. Cooling increases the solubility of oxygen within water which could serve as a negative feedback by increasing remineralisation rates at higher dissolved oxygen levels. Alternatively, respiration reactions slow significantly with lower temperature which may act as a positive feedback. Our model serves only to isolate the effect of clay mineralogy and SSA over Earth's climate, rather than act as a complete model for sedimentation, ocean chemistry, redox, and preservation on the continental margin.

We investigate the magnitude of changes induced by SSA driven OC preservation using a simple one-box model which couples the global fraction of exposed felsic, mafic, and ultramafic rocks, to clay formation, silicate weathering and pCO$_2$. The formation of clays is governed by the descriptions presented above while all other relationships are simplified to power laws or Arrhenius relationships.

Carbon Box Model

Our model follows the work of (9). The evolution of the mass of C in the ocean-atmosphere system, M_c, is a balance of influxes and outfluxes:

$$\Delta M_c/\Delta t = F_v - F_{sw} - F_{org} \tag{M5}$$

F_v is the flux of C from volcanic outgassing, metamorphic CO$_2$ release, and organic carbon/pyrite weathering. Today, this value is poorly constrained. We choose 200 MT/yr (e.g., 50, 51).

F_{sw} is the flux of C from ocean-atmosphere to lithosphere due to the precipitation of carbonate minerals from silicate-derived cations. F_{sw} is a function of both lithology and pCO_2 according to Eq. M6

$$F_{sw} = k_{sw} \cdot \lambda \cdot pCO_2^{\beta} \quad \text{(M6)}$$

Where,

$$\lambda = \text{weatherability} = p_f + 3.1 \cdot p_m + 8.1 \cdot p_u \quad \text{(M7)}$$

p_f, p_m, p_u = protolith fraction of felsic, mafic, and ultramafic rock

β = silicate weathering exponent = 0.22 (52)

$$k_{sw} = 25 \text{ MT/yr} \quad \text{(M8)}$$

k_{sw} is chosen such that $F_{sw} \approx 0.65\ F_v$ at pre-industrial conditions of pCO_2 = 280ppm and λ = 1.06.

Calculating pCO_2 requires assumptions about carbonate saturation in the ocean. Over the long-timescales we consider here, we treat the sum of ocean [Mg] + [Ca] to be constant and that M_c is dominantly HCO_3^-. Given the residence time of Mg in the ocean is ~13 Myr, these simplifications are reasonable. However, our estimated changes in pCO_2 should be treated as approximations.

$$pCO_2(t) = 280ppm \cdot \left(\frac{M_c(t)}{M_c(0)}\right)^2 \quad \text{(M9)}$$

Where $M_c(0)$ is the mass of carbon in the modern ocean-atmosphere system, 38,600,000 MT (9).

F_{org} is calculated according to Eq. M10-M13. We consider only the sediments delivered to the continental margin and deltaic regions. F_{org} can be limited either by the supply of mineral surfaces or by the supply of phosphorus to the ocean and we use the minimum of those two constraints in calculating F_{org} (Eq. M13).

Today, two thirds of modern sediment delivery is from the mafic, tectonically active regions that constitute southeast Asia and Oceania (53), suggesting that ophiolite obduction would increase global sedimentation rates. Conservatively, we assume that while the SSA of sediment changes, the total sediment flux remains constant. Similarly, we take ω to reflect mean, global climate. In areas with high degrees of chemical weathering and low physical erosion rates, ω may be far greater than the global value, moving past $\omega=10^{-3.6}$, at which point SSA and OC burial would begin to decrease, limiting the effect of obduction (**Fig. 1, S1**). Our model results do not reflect the increased local weathering in the warm, rainy tropics compared to higher latitudes (54) and the outsized importance of tropical lithologies is not incorporated (7,8,54).

$$F_{os} = d \cdot F_{sed} \cdot TOC / 100 \quad \text{(M10)}$$

$$\text{SSA} = p_f \cdot G_s(\omega) + 3.1 \cdot p_m \cdot B_s(\omega) + 8.1 \cdot p_u \cdot P_s(\omega) \quad \text{(M11)}$$

$$F_{op} = 12 \cdot M_P \cdot C{:}P / 31 \quad \text{(M12)}$$

$$F_{org} = \min\{F_{os}, F_{op}\} \quad \text{(M13)}$$

519 F_{sed} = global sediment flux = 14030 MT/yr (55)
520 d = nearshore/deltaic fraction of sediment flux = 0.3 (56)
521 F_{os} = SSA limited OC burial
522 F_{op} = Phosphorus limited OC burial
523 M_P = mass of available phosphorus in ocean

524 Where G_s, B_s, and P_s, are the numerical functions derived from mineral weathering laws which
525 relate ω to SSA as described above and shown in **Fig. 1D**. TOC is linked to SSA via Eq. M2. The
526 values of 3.1 and 8.1 which appear in Eq. M7 and Eq. M11 parameterise the silicate weathering
527 rates of mafic and ultramafic rocks, relative to felsic rocks, derived from the molar abundance of
528 Ca and Mg (33,57,58). The constants 12 and 31 reflect the molar mass of carbon and phosphorus,
529 respectively. ω is coupled to climate by the Arrhenius relationship (Eq. M14) and temperature is
530 approximated by a climate sensitivity equation (Eq. M15, 59).

$$\omega = \omega_0 \, e^{-\frac{E_a}{R}(\frac{1}{T} - \frac{1}{T_0})} \tag{M14}$$

$$T = T_0 + S \log_2(\frac{pCO_2}{pCO_2(0)}) \tag{M15}$$

531 S = Climate sensitivity = 3 K (60)

532 T_0 = pre-industrial average temperature = 298 K

533 $p\mathrm{CO_2}(0)$ = pre-industrial $p\mathrm{CO_2}$ = 280 ppm

534 E_a = activation energy = 74.9 kJ (6)

535 R = gas constant = 8.314 kJ/K/mol

536 ω_0 = reference weathering degree = 10^{-4}

537 We constrain ω_0 by compiling mineralogy from over 55,000 DSDP smear slides. By taking the
538 mean modal mineralogy, we find that the terrigenous portion consists primarily of clays, silica,
539 feldspar, and iron oxides (**Fig. S16**). The presence of 7.5% feldspar and 0.5% pyroxene places ω_0
540 between 10^{-5} and 10^{-3}. We use 10^{-4} for the results presented in **Fig. 2** and present a sensitivity test
541 in **Fig. S17**.
542 M_P is modelled similarly to M_C (Eq. M5) but governed only by the riverine flux, F_{P_SW}, and
543 OC burial divided by the buried C:P ratio.

$$F_{P\_SW} = 0.7 \cdot F_{sw} \cdot (31 / 12) \cdot (p_f \cdot 0.0111 + p_m \cdot 0.0071 \cdot 3.1 + p_u \cdot 0.00069 \cdot 8.1) / \lambda \tag{M16}$$

$$F_{P\_OC} = F_{org} / \mathrm{C{:}P} \cdot 31 / 12 \tag{M17}$$

$$C{:}P = 106 + (C{:}P_{max} - 106) \cdot e^{-20\frac{M_P}{M_P(0)}} \quad \text{(M18)}$$

The factor of 0.7 in Eq. M16 reflects the fraction of riverine phosphorus that is bioavailable (e.g., 61, 62), while the constants 0.0111, 0.0071, and 0.00069 are the molar ratios of P to Ca + Mg in felsic, mafic, and ultramafic rocks, respectively. In **Fig. 2** we vary $C{:}P_{max}$. The value -20 in Eq. M18 is a decay constant designed to maintain the Redfield ratio outside of very low values of M_P (**Fig. S18**). $M_P(0)$ is set as $1.2 \cdot 10^5$, derived from a steady-state OC burial of 70 MT/yr and a residence time of 69,000 yr (41). Given our model's lack of negative feedbacks for high phosphorus concentrations, we artificially impose an upper limit of $2 \cdot 10^5$. Sedimentary deposits of phosphate, which are common in the rock record but minor in the modern ocean, provide a pathway by which excess phosphorus is removed from the ocean (63).

Assuming carbonate minerals precipitate without carbon isotopic fractionation, the $\delta^{13}C$ of the ocean-atmosphere system through time is controlled by the fluxes F_V and F_{org}, as well as the size of the carbon reservoir:

$$\Delta\delta^{13}C/\Delta t = 1 / M \cdot ((F_V \cdot (\delta_V - \delta^{13}C)) - F_{org} \cdot \delta_{org}) \quad \text{(M19)}$$

In Eq. M19, δ_V is the combined carbon isotopic ratio of volcanic outgassing (traditionally -5‰) and organic carbon weathering (traditionally -22‰), which we set constant at -9‰ to achieve a steady state $\delta^{13}C$ around 0‰ (9). δ_{org} is the fractionation of carbon, relative to the oceanic value, via photosynthesis which we hold at -25‰ (64).

Compilation of Natural Records

Mean $\delta^{13}C$ excursions were calculated from the chemostratigraphic sections in **Table S5** and are used in **Fig. 3.** The magnitude of each excursion was chosen by eye. Representative sections are displayed in **Fig. 3B** and **Fig. S2** and were chosen due to their age constraints and higher temporal resolution. Our model curves are scaled uniformly in time to qualitatively match the shown sections. Approximate timing of the expansion of icesheets is shown on the lower bars. Semi-transparent coloured bars represent a prolonged end-member chronology, while opaque bars represent an abrupt end-member **(Table S4)**. We linearly interpolated ages for both glaciations and isotopic records between the known ages listed in **Table S3**, **S4**. The resultant time-evolution is poorly constrained, with some sections only tied by two age estimates.

The Permo-Carboniferous $\delta^{13}C$ range is derived from the data of (10). We use change-point analysis of a smoothed spline (smoothing parameter 0.1) through the data to find the onset of the $\delta^{13}C$ excursion at 324.4 Ma and plateau at 308.0 Ma. We subtract each $\delta^{13}C$ datum with age 324.4 ± 1 Ma (n = 30) from each $\delta^{13}C$ datum with age 308.0 ± 1 Ma (n = 70) and take the median and 1σ range of the resultant values.

We calculate the ophiolite length change for each glaciation by interpolating the suture lengths of (8) at 0.1 Ma resolution and subtracting the pre-glacial and post-glacial suture lengths from the syn-glacial suture lengths. We use the ages of the glaciations given in **Table S3**. For the suture lengths which follow the Permo-Carboniferous we use 255 Ma as the minimum age.

Analysis of Shale Geochemistry

We queried the Stanford Geochemistry and Palaeoenvironments database (40), filtering for "shale" as the lithology. A total of 7820 samples contained data for Cr, Al_2O_3, and TOC; 6679 samples contained data for Co, Al_2O_3, and TOC; and 7755 contained data for Ni, Al_2O_3, and TOC.

We consider the ratio Cr/Al as a simple measure of ultramafic provenance. To make systematic variations more visible, we construct bins of Cr/Al and calculate the distribution of TOC within those bins. Any bin with fewer than 15 samples is ignored. In **Fig. 4A** we show the median Cr/Al, the median TOC, and the 1σ range in TOC values (16^{th} to 84^{th} quantiles). **Fig. 4B** overlays the Phanerozoic time variation in shale Cr/Al on the abrupt and prolonged end-member glaciation chronologies (**Table S3)**. Similar relationships are shown in **Fig. S11** for Co/Al and Ni/Al.

Data Availability

Compiled SSA and TOC data are available within the Supplementary Data as Table S6. Geologic constraints are available within the Supplementary Data as Table S7. SGP data were downloaded on October 3rd, 2022, filtering for the following lithologies: shale, mudstone, siltstone. Iron and phosphorus data were downloaded from EarthChem on March 19th, 2022, filtering all igneous rock analyses for which SiO_2, FeO, and P_2O_5 are present. The igneous and sedimentary geochemical data are reproduced within the Supplementary Data and are available at https://doi.org/10.6084/m9.figshare.24433012.

Code Availability

MATLAB functions are available for both the weathering model, weatherRock.m, and the carbon box model, carbonPhosphorusModel.m. The functions can be found at https://doi.org/10.6084/m9.figshare.24433012.

Methods-only References

48. Rivero Crespo, Miguel A., Dolores Pereira Gómez, María V. Villa García, José M. Gallardo Amores, and Vicente Sánchez Escribano. "Characterization of serpentines from different regions by transmission electron microscopy, X-ray diffraction, BET specific surface area and vibrational and electronic spectroscopy." *Fibers* 7, no. 5 (2019): 47.
49. Young, R. *Soil properties and behaviour*. Vol. 5. Elsevier, 2012.
50. Burton, Michael R., Georgina M. Sawyer, and Domenico Granieri. "Deep carbon emissions from volcanoes." *Reviews in Mineralogy and Geochemistry* 75, no. 1 (2013): 323-354.
51. Soulet, Guillaume, Robert G. Hilton, Mark H. Garnett, Tobias Roylands, Sébastien Klotz, Thomas Croissant, Mathieu Dellinger, and Caroline Le Bouteiller. "Temperature control on CO_2 emissions from the weathering of sedimentary rocks." *Nature Geoscience* 14, no. 9 (2021): 665-671.
52. Berner, Robert A., Antonio C. Lasaga, and Robert M. Garrels. "Carbonate-silicate geochemical cycle and its effect on atmospheric carbon dioxide over the past 100 million years." *Am. J. Sci.;(United States)* 283, no. 7 (1983).
53. Milliman, John D., and Katherine L. Farnsworth. *River discharge to the coastal ocean: a global synthesis*. Cambridge University Press, 2013.
54. Kent, Dennis V., and G. Muttoni. "Modulation of Late Cretaceous and Cenozoic climate by variable drawdown of atmospheric pCO_2 from weathering of basaltic provinces on continents drifting through the equatorial humid belt." *Climate of the Past* 9, no. 2 (2013): 525-546.
55. Syvitski, James PM, Charles J. Vorosmarty, Albert J. Kettner, and Pamela Green. "Impact of humans on the flux of terrestrial sediment to the global coastal ocean." *science* 308, no. 5720 (2005): 376-380.
56. Kuehl, Steven A., Mead A. Allison, Steven L. Goodbred, and Herman N. Kudrass. "The Ganges-Brahmaputra Delta." *Special Publication-SEPM* 83 (2005): 413.
57. Rudnick, R. L., S. Gao, H. D. Holland, and K. K. Turekian. "Composition of the continental crust." *The crust* 3 (2003): 1-64.
58. Gale, Allison, Colleen A. Dalton, Charles H. Langmuir, Yongjun Su, and Jean-Guy Schilling. "The mean composition of ocean ridge basalts." *Geochemistry, Geophysics, Geosystems* 14, no. 3 (2013): 489-518.
59. Arrhenius, Svante. "XXXI. On the influence of carbonic acid in the air upon the temperature of the ground." *The London, Edinburgh, and Dublin Philosophical Magazine and Journal of Science* 41, no. 251 (1896): 237-276.
60. Sherwood, Steven C., Sandrine Bony, and Jean-Louis Dufresne. "Spread in model climate sensitivity traced to atmospheric convective mixing." *Nature* 505, no. 7481 (2014): 37-42.

61. Stepanauskas, Ramûnas, Niels OG JØrgensen, Ole R. Eigaard, Audrius Žvikas, Lars J. Tranvik, and Lars Leonardson. "Summer inputs of riverine nutrients to the Baltic Sea: bioavailability and eutrophication relevance." *Ecological monographs* 72, no. 4 (2002): 579-597.
62. Pacini, Nic, and René Gächter. "Speciation of riverine particulate phosphorus during rain events." *Biogeochemistry* 47, no. 1 (1999): 87-109.
63. Frohlich, P. N., M. L. Bender, N. A. Luedtke, G. R. Heath, and T. DeVries. "Marine phosphorus cycle." *Am. J. Sci.;(United States)* 282, no. 4 (1982).
64. Hayes, John M., Harald Strauss, and Alan J. Kaufman. "The abundance of ^{13}C in marine organic matter and isotopic fractionation in the global biogeochemical cycle of carbon during the past 800 Ma." *Chemical Geology* 161, no. 1-3 (1999): 103-125.